Journal of Materials Science & Technology 260 (2026) 279–289

Contents lists available at ScienceDirect

Journal of Materials Science & Technology

journal homepage: www.elsevier.com/locate/jmst

Research Article

Spin-polarized high-entropy pyrophosphates breaking the activity-stability trade-off for ultra-stable alkaline seawater oxidation at industrial-scale current densities

Hai Li[a,b,1], Mingyu Wang[a,1], Xiaoliang Zhang[c], Wen-Qiang Xie[a,b], Hongliang Dong[d], Yangyang Liu[a,b], Youpeng Li[a,b], Yifeng Wang[a,b], Zhun Tang[a,b], Rongbin Lin[a,b], Aimin Yu[e], Dong-Sheng Li[f], Weiwei Li[a,b,*], Chenghua Sun[e,*], Jinchun Tu[a,b,*]

[a] State Key Laboratory of Tropic Ocean Engineering Materials and Materials Evaluation, Hainan University, Haikou 570228, China
[b] School of Materials Science and Engineering, Hainan University, Haikou 570228, China
[c] School of Electronic Engineering, Tongling University, Tongling 244061, China
[d] Center for High Pressure Science and Technology Advanced Research, Shanghai Key Laboratory of Material Frontiers Research in Extreme Environments (MFree), Institute for Shanghai Advanced Research in Physical Sciences (SHARPS), Shanghai 201203, China
[e] Department of Chemistry and Biology, Swinburne University of Technology, Hawthorn, VIC 3122, Australia
[f] College of Materials and Chemical Engineering, Key Laboratory of Inorganic Nonmetallic Crystalline and Energy Conversion Materials, China Three Gorges University, Yichang 443002, China

ARTICLE INFO

Article history:
Received 25 June 2025
Revised 17 September 2025
Accepted 17 September 2025
Available online 11 October 2025

Keywords:
Seawater electrolysis
High-entropy pyrophosphates
Spin engineering
Magnetic superexchange interaction
Hydrogen-bonded network

ABSTRACT

Developing electrocatalysts with ingenious active site-environment interactions for robust oxygen evolution reaction in alkaline seawater is essential for sustainable hydrogen production under industrial conditions, yet remains a significant challenge. Herein, we present a high-entropy amorphous pyrophosphate, $FeCoNiMnPO_x$, that serves as a highly active and durable electrocatalyst for alkaline seawater oxidation at large current densities. Our strategy leverages spin-state engineering of active metal sites by modulating oxygen vacancy concentrations via magnetic superexchange interactions. We found that four-coordinated Fe sites in $FeCoNiMnPO_x$ facilitate the highest spin state transition, boosting dense π-bonding with oxygen intermediates, resulting in a near-optimal activity descriptor of $\Delta G_{O^*} - \Delta G_{OH^*} = 1.76$ eV. Such an optimized catalyst achieves a low overpotential of 299 mV at 400 mA cm^{-2} and exhibits exceptional stability, maintaining performance for over 1000 h at 500 mA cm^{-2} in alkaline seawater. This exceptional stability stems from the formation of a robust hydrogen-bonded network of four-coordinated interfacial water, which effectively repels detrimental chloride ions, mitigating catalyst corrosion and ensuring long-term durability. This work underscores the critical role of spin-state engineering in electrocatalysis and provides a novel pathway for designing highly durable electrocatalysts towards sustainable hydrogen production from seawater.

1. Introduction

Seawater electrolysis offers a viable pathway to alleviate freshwater scarcity while facilitating large-scale hydrogen production, particularly in arid regions [1,2]. However, chloride-induced corrosion of electrodes presents a formidable challenge [3]. This issue is most pronounced at the anode, where sluggish oxygen evolution reaction (OER) kinetics and structural degradation under high current densities lead to compromised efficiency and durability [4–6]. Conventional corrosion-mitigation strategies through passivation layers, ion-selective barriers, or corrosion-resistant elements incorporation inevitably compromise catalytic activity via active site masking or elemental leaching [7–9]. Critically, enhancing catalytic activity often exacerbates structural instability, rendering catalysts more susceptible to Cl^--induced degradation [3]. Recent studies suggest that in-situ generated oxyanions (e.g., molybdates, sulfates, and phosphates) exhibit chloride-repelling capabilities through interfacial charge redistribution, enhancing activity and long-term stability [10–12]. However, sustaining such dynamic anion shielding requires precise stabilization of the host matrix against oxyanions' continuous leaching over extended operation at

* Corresponding authors.
E-mail addresses: weiwei.li@hainanu.edu.cn (W. Li), chenghuasun@swin.edu.au (C. Sun), tujinchun@hainanu.edu.cn (J. Tu).
[1] These authors contributed equally to this work.

https://doi.org/10.1016/j.jmst.2025.09.047
1005-0302/

high current densities [13,14]. Therefore, developing anode materials with inherent resistance to Cl^- corrosion to balance high activity and long stability is a promising but unresolved challenge in seawater electrolysis.

High-entropy materials, incorporating multiple transition metals with diverse orbital configurations, are highly promising catalysts that may balance activity and stability due to their high-entropy cocktail effect [15,16]. However, traditional modulation strategies, such as defects and doping, often encounter difficulties in chloride-rich seawater environments due to the averaging effect of their *d*-band [4]. Recent advances in spin-state engineering provide a transformative strategy to circumvent these limitations by manipulating the *d*-orbital occupancy of active centers, thereby regulating intermediate adsorption/desorption kinetics and corrosion resistance through spin-selective electron transfer [17,18]. Unlike conventional high-entropy oxides limited by rigid oxygen sublattices, high-entropy pyrophosphates ($M_2P_2O_7$) are a novel class of spin-tunable electrocatalysts, where the unique $P_2O_7^{4-}$ framework enables dynamic modulation of active center coordination geometry through oxygen vacancy (O_v) concentration [19–21]. Moreover, the phosphate matrix not only enhances structural integrity through strong covalent P-O bonding but also facilitates spin-polarized interactions via π-conjugated PO_4 units [22]. Despite their potential, achieving simultaneously high activity and stability in seawater electrolysis through spin modulation remains challenging.

To address these challenges, we propose an innovative strategy that employs spin-state engineering to introduce dense π-bonding interactions by regulating O_v concentrations in high-entropy amorphous FeCoNiMnPO$_x$ (HE-APOs), enriching surface OH^- ions, and mitigating Cl^--induced corrosion. As demonstrated below, O_v increment induces a four-coordinated Fe configuration, promoting low-spin to high-spin transition. High-spin states facilitate π-bond formation via magnetic superexchange interactions, which stabilize oxygenated intermediates while enriching hydroxide ion concentrations. This, in turn, promotes the formation of four-coordinated hydrogen-bonded interfacial water, establishing a strong hydrogen-bonded network that mitigates Cl^--induced corrosion and enhances OER performance in seawater electrolysis. Consequently, the optimized HE-APOs catalyst exhibits a remarkably low overpotential of 299 mV at 400 mA cm^{-2} and exceptional durability, sustaining the performance for over 1000 h at 500 mA cm^{-2}. Our study highlights the transformative role of spin-state modulation in catalysis, offering a new paradigm for designing advanced electrocatalysts with molecular-level selectivity for sustainable hydrogen production.

2. Materials and methods

2.1. Chemicals and materials

$Fe(CO_2CH_3)_2{\cdot}4H_2O$ (98.5%), $Co(NO_3)_2{\cdot}6H_2O$ (99.0%), $Ni(NO_3)_2{\cdot}6H_2O$ (99.0%), $Mn(NO_3)_2{\cdot}4H_2O$ (98.5%), ammonium fluoride (NH_4F, 99.0%), N,N-dimethylformamide (DMF), 2,5-dihydroxyterephthalic acid, N,N-diethyl-1,4-phenylenediamine sulfate (DPD), ethanol, KOH, dilute sulfuric acid (99.0%), and hydrogen peroxide (99.0%) were purchased from Shanghai Macklin Biochemical Technology Co., LTD. IrO_2 (98.5%), NaH_2PO_2 H_2O (99.0%), $Na_2S{\cdot}9H_2O$ (99.0%), and Nafion (5 wt.%) were obtained from Johnson Matthey and Dupont, respectively. All chemicals and reagents were used without further purification. Carbon cloth (CC) was purchased from Kunshan Longsheng. Deionized water (resistivity: 18.3 MΩ cm) was used for the reaction and pure aqueous solution configuration. The seawater solution used for the tests was collected from Haikou Bay, Haikou, Hainan Province, China.

2.2. Synthesis of FeCoNiMn metal-organic framework (MOF), HE-APOs, and optimized HE-APOs-18

FeCoNiMn MOF was synthesized on CC (4.0 cm × 3.0 cm) using a simple hydrothermal method. First, the CC was soaked in a solution of dilute sulfuric acid and hydrogen peroxide (3:1 v/v) for 1 h. After soaking, the CC was thoroughly washed and dried, preparing it for use as a template in the MOF synthesis. For the synthesis, equimolar amounts (0.25 mmol each) of metal nitrates—$Fe(CO_2CH_3)_2{\cdot}4H_2O$, $Co(NO_3)_2{\cdot}6H_2O$, $Ni(NO_3)_2{\cdot}6H_2O$, $Mn(NO_3)_2{\cdot}4H_2O$—were dissolved in 45.0 mL of dimethylformamide (DMF), along with 0.34 mmol of 2,5-dihydroxyterephthalic acid, 2.7 mL of anhydrous ethanol, and 2.7 mL of deionized water. After 30 min of magnetic stirring, the mixture and the CC were transferred to a 100.0 mL Teflon-lined stainless-steel autoclave for a hydrothermal reaction at 120 °C for 30 h. Once the reaction was complete and cooled to room temperature, the FeCoNiMn MOF was washed several times with DMF and ethanol, then dried at 60 °C for 12 h.

Amorphous HE-APOs were synthesized using a standard phosphating process. First, 0.5 g of $NaH_2PO_2{\cdot}H_2O$ and a piece of FeCoNiMn MOF (4 cm × 3 cm) were placed in the upstream and downstream sections of a tube furnace, respectively. The furnace was then heated to 400 °C over 75 min under a high-purity argon (Ar) atmosphere and maintained at that temperature for 4 h. To investigate the effect of calcination temperature on electrocatalytic performance, the calcination temperature was adjusted to 350 and 450 °C, respectively, for comparison. After cooling to room temperature, HE-APOs were collected.

The HE-APOs-18 was synthesized using a simple etching method. A piece of HE-APOs was soaked in 30.0 mL of an 8.3 mmol/L $Na_2S{\cdot}9H_2O$ solution for 30 min. This etching process is driven by the reductive action of aqueous sulfide species (S^{2-}/HS^-), which selectively remove surface lattice oxygen from the HE-APOs to create a controlled concentration of oxygen vacancies. The sample was then dried in a vacuum oven at 60 °C for 12 h. To examine the influence of etching time on electrocatalytic performance, times were adjusted to 15 and 60 min. Additionally, the effect of $Na_2S{\cdot}9H_2O$ solution concentration was studied by varying concentrations to 6.3, 10.3, and 12.3 mmol/L.

2.3. Materials characterization

The microstructure and morphology of the catalysts were analyzed using a scanning electron microscope (SEM, CrossBeam 350, ZEISS, 5 kV) and a transmission electron microscope (TEM, Tecnai G2 F30). X-ray diffraction (XRD) patterns were collected over a 5° to 80° range using a Smart Lab XRD system with Cu-Kα radiation to determine the crystalline phases. Raman spectra were recorded using a laser Raman spectrometer (in Via, Renishaw plc) with a 514 nm wavelength. Fourier transform infrared spectroscopy (FT-IR, T27, Bruker) was used to identify chemical bonding. Electron paramagnetic resonance (EPR) measurements were performed using a BRUKER EMXPLUS spectrometer. The contents of Fe, Co, Ni, and Mn were obtained by inductively coupled plasma emission spectroscopy (ICP-OES) conducted on an Agilent 720ES/iCAP PRO instrument. X-ray photoelectron spectroscopy (XPS, NexsaG2) was used to determine the chemical states of the catalysts, with all XPS spectra calibrated to the C 1*s* line at 284.8 eV. Fe K-edge X-ray absorption spectroscopy (XAS) measurements were performed at the beamline station BL17B1 of Shanghai Synchrotron Radiation Facility (SSRF) using an X-ray fluorescence signal detector. Then, the obtained XAS data were processed using the Athena and Artemis packages [23]. The effective magnetic moment (μ_{eff}) is calculated according to the following Eq. (1) [24]:

$$\mu_{eff} = \sqrt{8C}\mu_B \quad (1)$$

where C is the Curie constant and μ_B is the Bohr magneton, a fundamental physical constant representing the magnetic moment of an electron.

$$\chi = C/(T - \Theta) \tag{2}$$

where Θ represents the Curie-Weiss temperature and the slope of the χ^{-1}-T curve. T is the absolute temperature at which the measurement is taken, expressed in Kelvin (K). Susceptibility (χ) can be obtained from the following Eq. (3):

$$\chi = M/H \tag{3}$$

where M is the magnetization of the material (the magnetic moment per unit volume or mass, representing the material's response to the field), and H is the strength of the applied external magnetic field.

2.4. Electrochemical measurements

Room-temperature electrochemical tests were conducted using a Bio-Logic multichannel electrochemical workstation (VMP-300). For OER assessments, a standard three-electrode setup was used: the prepared samples served as the working electrode, a graphite rod as the counter electrode, and a standard Hg/HgO electrode as the reference. Three different electrolytes were tested: 1.0 M KOH, 1.0 M KOH + 0.5 M NaCl, and 1.0 M KOH + Seawater, all with a pH of approximately 14. The seawater was sourced from Haikou Bay near Haikou, Hainan, China. OER polarization curves were measured at a scan rate of 5 mV s^{-1}. The solution resistance (R_s) was obtained from high-frequency electrochemical impedance spectroscopy (EIS) measurements at the corresponding electrolyte conditions. All polarization curve data were reported with iR compensation applied automatically using a current-interrupt model on the electrochemical workstation. A 90% iR correction was adopted to minimize the influence of ohmic drop while avoiding possible overcompensation artifacts. The residual uncompensated resistance (< 10%) ensures that the reported overpotentials reliably reflect the intrinsic catalytic behavior. All potentials were further converted to the reversible hydrogen electrode (RHE) scale for comparison. All potentials measured against Hg/HgO were converted to the RHE using the Nernst equation $E(\text{RHE}) = E(\text{Hg/HgO}) + 0.059 \times \text{pH} + 0.098$ [25].

Double-layer capacitance (C_{dl}) values were determined from CV curves obtained at various scan rates ranging from 20 to 160 mV s^{-1}, in increments of 20 mV s^{-1}. The electrochemical surface area (ECSA) was estimated by normalizing the C_{dl} with a standard specific capacitance (C_s) of 0.04 mF cm^{-2} in 1.0 M alkaline electrolyte. The intrinsic activity normalized by ECSA was calculated using the following Eq. (4):

$$j_{ECSA} = j/\text{ECSA} = j/(C_{dl}/C_S) \tag{4}$$

EIS were recorded at an overpotential of 274 mV across frequencies from 0.01 Hz to 100 kHz [26]. Stability evaluations were conducted under a constant current density of 500 mA cm^{-2}. The turnover frequency (TOF) was calculated using the following Eq. (5) for OER [27]:

$$\text{TOF} = j/(4 \times F \times n) \tag{5}$$

The O_2 faradaic efficiency was determined using Faraday's law in conjunction with the ideal gas Eqs. (6–9) [10]:

$$j \times t = n \times z \times F \tag{6}$$

$$p \times V = n \times R \times T \tag{7}$$

$$V_{theor} = \frac{j \times R \times T}{z \times F \times p} \tag{8}$$

$$\text{FE}(\%) = \frac{V_{nominal}}{V_{theor}} \tag{9}$$

where j is the applied current in ampere (A); t is the time in second (s); n is the number of substances in molarity (mol); z of 4 represents the electrons transferred for OER; F, p, R, and T are the faradaic constant of 96,485.33 s A mol^{-1}, the atmospheric pressure of 101000 Pa, the ideal gas constant of 8.314 kg m^2 s^{-2} mol^{-1} K^{-1}, and temperature 298.15 K, respectively; V is the gas volume in cubic meter (m^3), and FE is the gas evolution rate of O_2 in cubic meter per second (m^3 s^{-1}).

2.5. Sodium hypochlorite detection experiment

The hypochlorite content in seawater electrolytes, after undergoing a 100 h OER test at 500 mA cm^{-2}, was quantified using the DPD colorimetric method. The pH of a 20 mL sample was first brought to 6–7 with HCl. Subsequently, the addition of 5 mL of DPD solution (1.0 g L^{-1}) initiated the formation of colored Worcester dye from the reaction with hypochlorite. The resulting absorbance was measured at a wavelength of 550 nm on a Shimadzu UV-1780 spectrophotometer.

2.6. Density functional theory (DFT) calculation

All the calculations were performed in the framework of the DFT with the projector augmented plane-wave method, as implemented in the Vienna ab initio simulation package [28]. We used the generalized gradient approximation with the Pedrew-Burke-Ernzerhof (PBE) function and Hubbard U corrections (4.6, 5.3, 3.3, and 6.2 eV for treating Mn, Fe, Co, and Ni 3d orbitals) were introduced to consider the self-interaction error of transition metals [29]. The cut-off energy for the plane wave is set to 500 eV. The energy criterion is set to 10^{-5} eV in the iterative solution of the Kohn-Sham equation. The vacuum layer of 15 Å is added perpendicular to the sheet to avoid artificial interaction between periodic images. The Brillouin zone integration is performed using a 2 × 2 × 1 k-mesh. All the structures are relaxed until the residual forces on the atoms have declined to less than 0.01 eV/Å.

3. Results and discussion

3.1. Synthesis and structural characterizations

The high-entropy amorphous phosphorus oxides (HE-APOs) with various oxygen vacancy (O_v) concentrations were synthesized via a three-step process involving hydrothermal treatment, phosphorization, and subsequent etching, as schematically depicted in Fig. 1(a). Initially, Fe-Co-Ni-Mn-based metal-organic frameworks (FeCoNiMn MOFs) are first nucleated in-situ on CC via coordination between the metal ions and the oxygen-containing functional groups of 2,5-dihydroxyterephthalic acid. These MOFs are then reacted with NaH_2PO_2 at high temperature, where PO_4^{3-} species undergo condensation to form $P_2O_7^{4-}$, resulting in the phosphorized HE-APOs. Finally, the S^{2-}/HS^- ions generated from the dissolution act as a mild reducing agent to selectively remove surface lattice oxygen from the HE-APOs, thereby creating O_v. By tuning the concentration of $Na_2S{\cdot}9H_2O$ and the etching time, we precisely controlled the O_v concentration to obtain the optimized HE-APOs catalyst.

Morphological transformations during phosphorization and etching processes were examined via SEM. The initial spherical MOF structure (~1 μm diameter) with needle-like features (Fig. S1 in the Supplementary Materials) evolved into a rough surface covered with ~80 nm pellets post-etching (Fig. 1(b–d)). This structural

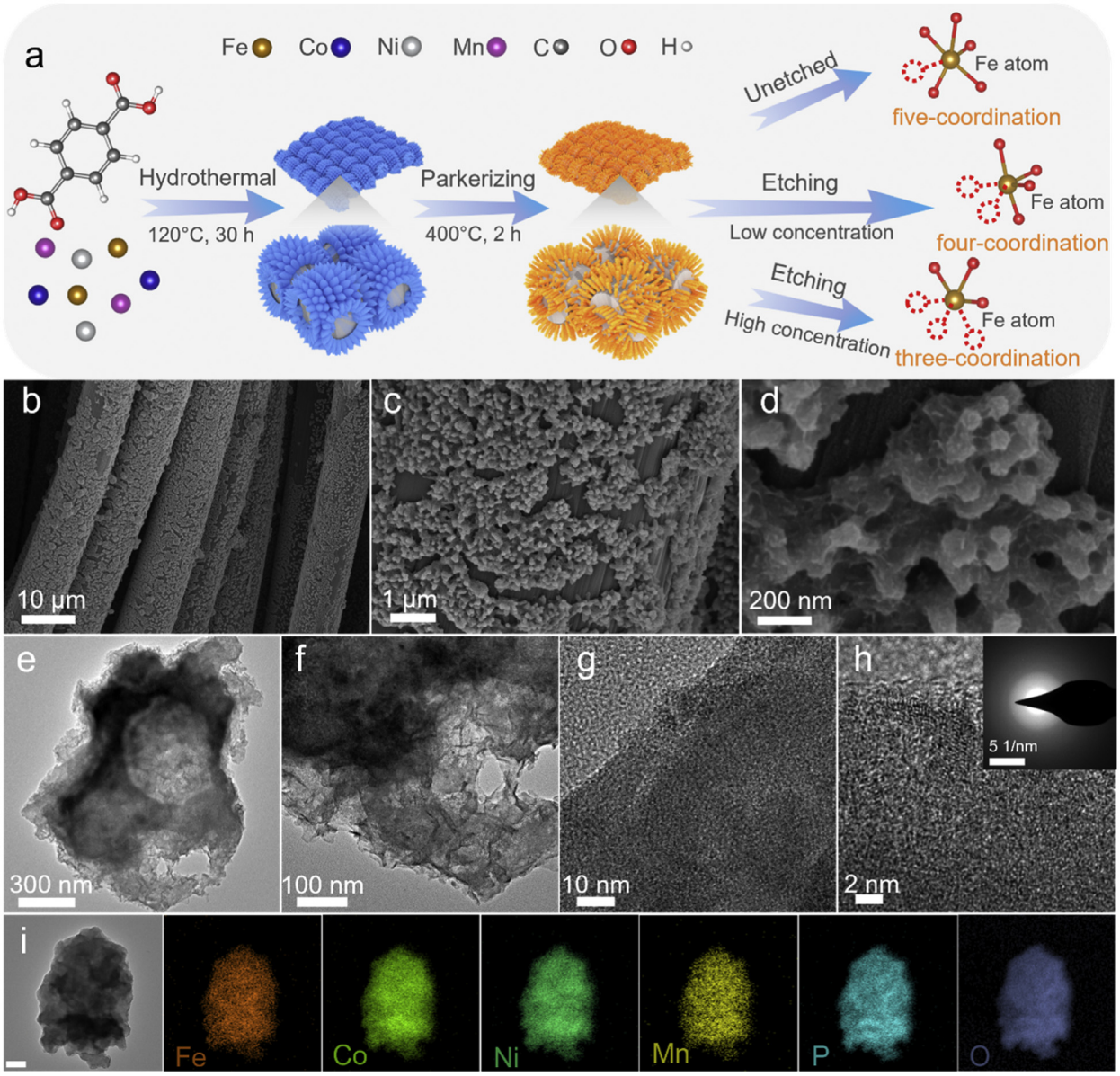

Fig. 1. Fabrication procedure and structural characterization of optimized HE-APOs. (a) Schematic diagram of the optimized HE-APOs. Morphology characterization: (b–d) SEM images, (e–h) TEM and HRTEM images (inset, SAED image), and (i) corresponding elemental mapping images, scale bar, 200 nm.

modification enhances surface area and active site exposure. TEM images (Fig. 1(e–g)) confirm the amorphous nature of the material, as evidenced by the absence of lattice fringes, further supported by high-resolution TEM (HRTEM) and selected area electron diffraction (SAED, Fig. 1(h)). Energy-dispersive X-ray spectroscopy (EDX) mapping (Fig. 1(i)) demonstrates the uniform distribution of Fe, Co, Ni, Mn, P, and O elements, with atomic ratios of 3.8:4.8:4.4:1.9:12.8:72.4 (Fig. S2). These findings were corroborated by ICP-OES (Fig. S3).

To further verify the synthesis of optimized HE-APOs, XRD, Raman spectroscopy, and FT-IR spectroscopy were employed to characterize the crystal structure and vibrational modes. XRD patterns confirm the amorphous nature (Fig. S4), while Raman spectra (Fig. S5) exhibit D and G bands associated with carbon-carbon (C-C) vibrations, consistent with XRD results [30]. FT-IR spectra (Fig. S6) display peaks at 1080.1 cm^{-1} (P-O antisymmetric stretching) and 541.9 cm^{-1} (M-O vibrations), confirming successful phosphorization [2,31]. Collectively, these results validate the successful synthesis of optimized HE-APOs, which are characterized by their rough, pellet-covered surfaces, amorphous structure, and uniform elemental distribution with near-equimolar metal cation composition.

To investigate the effects of etching conditions on the electronic structure, the concentration of the etching agent was systematically varied across a range of 0 to 12.3 mmol/L, specifically at 0, 6.3, 8.3, 10.3, and 12.3 mmol/L. The resulting chemical states and structural modifications were analyzed using XPS and EPR. The high-resolution O 1*s* spectra (Fig. 2(a)) reveal peaks at 531.2, 532.2, 533.4, and 534.2 eV, corresponding to metal-oxygen (M-O), phosphorus-oxygen (P-O), O_v, and adsorbed H_2O, respectively [32]. The O_v content systematically increases from 12% at 0 mmol/L to 25% at 12.3 mmol/L, accompanied by shifts to lower binding energies, indicating alterations in the local electronic environment (Tables S1–S5). To examine the effects of O_v on HE-APOs, we initiated with a baseline sample, HE-APOs-12, featuring 12% O_v. Subsequent samples were etched to increment O_v concentrations, designated as HE-APOs-16 (16% O_v), HE-APOs-18 (18% O_v), HE-APOs-21 (21% O_v), and HE-APOs-25 (25% O_v).

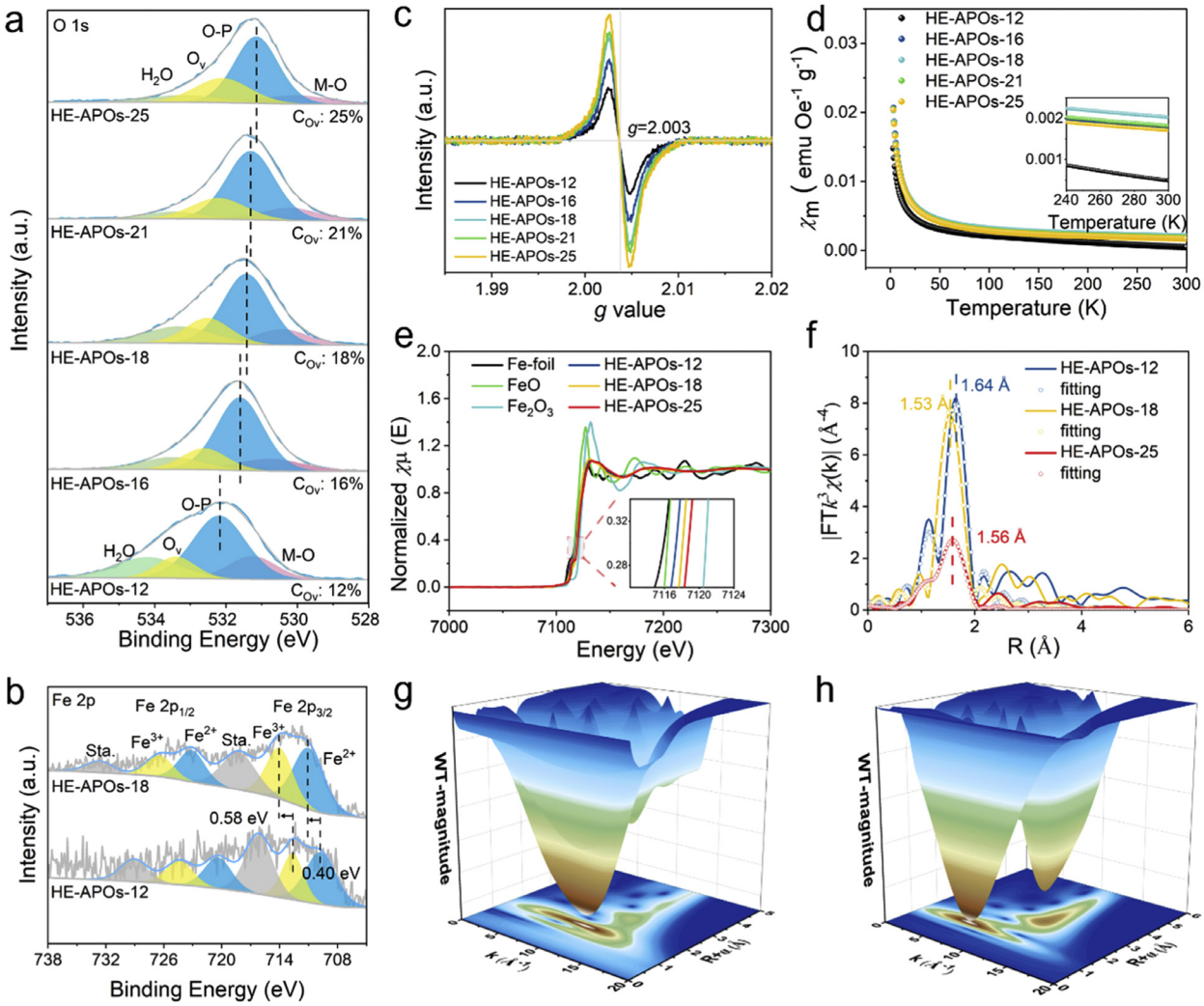

Fig. 2. (a) XPS of O 1*s* with different etching agent concentrations. (b) XPS of Fe 2*p*. (c) EPR with different etching agent concentrations. (d) M-T susceptibility χ_m–*T* curves. (e) Fe K-edge XANES spectra. (f) Fourier transform and fitting of k^3-weighted EXAFS oscillation. 3D contour WT-EXAFS plots of Fe K-edge: HE-APOs-12 (g) and HE-APOs-18 (h).

XPS survey spectra of HE-APOs-18 confirm the presence of expected elements (Fig. S7(a)). Quantitative analysis of this data reveals surface elemental ratios consistent with bulk compositions from ICP-OES (Fig. S3), confirming the compositional homogeneity of the catalyst and the absence of any detectable sulfur incorporation from the etching process (Table S6, Fig. S7(b)). In the Fe 2*p* XPS spectrum (Fig. 2(b)), peaks at 710.2/722.7 and 713.3/726.1 eV correspond to Fe^{2+} and Fe^{3+}, respectively [32,33]. The positive shift of these peaks with increasing O_v concentration suggests that the introduction of oxygen vacancies facilitates Fe to act as electron donors, facilitating the transformation of high-valent metal, which is essential for high catalytic activity. High-resolution XPS analysis of Mn, Co, and Ni (Fig. S8) shows binding energy shifts to lower values, indicating their function as electron acceptors and contributing to electron balance. Detailed fitting parameters for the high-resolution XPS spectra of Fe, Co, Ni, Mn, and P can be found in Tables S7–S16. This electron redistribution emphasizes Fe's role as the main active site and highlights the synergistic electronic effects within the high-entropy catalyst. The EPR spectra (Fig. 2(c)) exhibit a *g*-factor of 2.003, characteristic of O_v [34], with signal intensity increasing as the etching agent concentration increases, indicating a direct correlation between O_v content and etching conditions.

Magnetic susceptibility measurements further elucidated the role of O_v in modulating spin states. Temperature-dependent magnetization (M-T) curves (Fig. 2(d)) recorded under a 2 kOe field after zero-field cooling reveal that the plot of inverse susceptibility ($1/\chi_m$–*T*) versus temperature plots (Fig. S9) follow Curie-Weiss behavior above 200 K [35]. The effective magnetic moment (μ_{eff}) increases with O_v concentration, peaking at 3.15 μ_B at 18.0% O_v before declining at higher concentrations (Table S17). This trend highlights the presence of an optimal electron spin configuration and magnetic coupling at moderate O_v levels, which facilitates robust superexchange interactions across Fe-O-*M* bridges (*M* representing other cations), crucial for catalytic performance.

X-ray absorption fine structure (XAFS) analysis provides further insights into the impact of O_v on coordination and bonding structures. X-ray absorption near-edge structure (XANES, Fig. 2(e)) reveals an increase in Fe valence states from +2.27 in HE-APOs-12 to +2.44 in HE-APOs-18 and +2.60 in HE-APOs-25, consistent with XPS results. The emergence of a pronounced pre-edge feature in etched samples suggests significant alterations in geometric symmetry and coordination environments. Extended X-ray absorption fine structure (EXAFS, Fig. 2(f)) analysis demonstrates a progressive reduction in Fe-O bond lengths from 1.64 Å (HE-APOs-12) to 1.53 Å (HE-APOs-18), while the Fe-O coordination number decreases from 5.6 (HE-APOs-12) to 4.6 (HE-APOs-18) and further to 2.9 (HE-APOs-25) (Table S18), confirming the formation of a four-coordinated Fe environment at moderate O_v levels [24]. Wavelet transform (WT) analysis (Figs. 2(g and h) and S10) further substantiates these find-

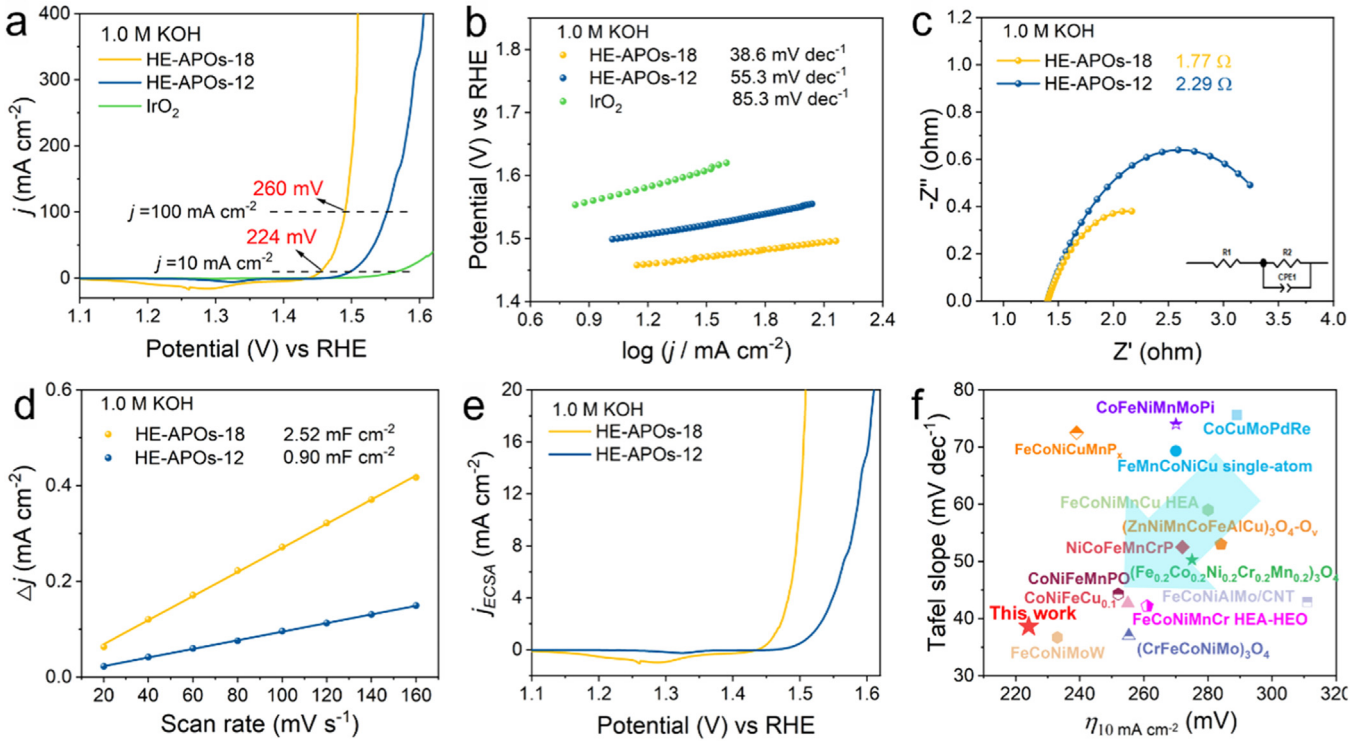

Fig. 3. Electrocatalytic OER performance of HE-APOs-18, HE-APOs-12, and IrO_2 samples in 1.0 M KOH solution. (a) LSV curves. (b) Tafel slope. (c) EIS spectra. (d) Charging current density differences plotted against scan rate. (e) ECSA normalized polarization curves. (f) The overpotential of HE-APOs-18 compared to other reported materials at 10 mA cm^{-2} in 1.0 M KOH.

ings, illustrating the evolution of local coordination as a function of O_v concentration.

Collectively, these results underscore the critical role of O_v in modulating spin states and the coordination environment of HE-APOs. As O_v concentration increases, the coordination number of metal centers decreases, and the spin state reaches its maximum at an 18% O_v concentration. Specifically, EXAFS revealed that the optimal catalyst featured a prevalence of four-coordinate Fe sites, a highly unsaturated geometry that was critical for binding intermediates. This structural transformation was accompanied by a synergistic, system-wide electronic redistribution, whereby Fe acted as an electron donor (valence increased) while Mn, Co, and Ni served as electron acceptors (valence decreased), as evidenced by both XPS and XANES. This highlighted that the four-coordinated Fe site, electronically optimized via hetero-element charge compensation, served as the primary active center for OER. Furthermore, the $P_2O_7^{4-}$ framework not only provided structural integrity but also mediated the strong magnetic superexchange interactions between the different metal cations, which were essential for stabilizing the catalytically crucial high-spin state of Fe. These findings highlighted the delicate balance between geometry, inter-element electronics, and spin coupling required for optimizing catalytic activity and stability in seawater electrolysis.

3.2. Electrochemical measurement of OER activities

The OER performance of the catalysts was rigorously evaluated in a 1.0 M KOH solution (pH = 14), with commercial IrO_2 on CC serving as the benchmark for comparison. Detailed optimization steps are provided in Figs. S11 and S12. The optimized results indicate that the OER activity is the most superior when the O_v concentration reaches 18%. Consequently, HE-APOs-18 were compared to unetched HE-APOs-12 and IrO_2 using linear sweep voltammetry (LSV, Fig. 3(a)). Specifically, HE-APOs-18 exhibits superior activity, achieving current densities of 10 and 100 mA cm^{-2} at overpotentials of 224 and 260 mV, respectively, outperforming both HE-APOs-12 (265 and 322 mV) and IrO_2 (336 mV at 10 mA cm^{-2}). To further investigate the kinetics and charge-transfer resistance (R_{ct}), Tafel slopes and R_{ct} values were examined. HE-APOs-18 achieves a Tafel slope of 38.6 mV dec^{-1}, lower than both HE-APOs-12 (55.3 mV dec^{-1}) and IrO_2 (85.3 mV dec^{-1}), indicating faster reaction kinetics (Fig. 3(b)). Additionally, HE-APOs-18 exhibits a reduced R_{ct} of 1.77 Ω compared to HE-APOs-12 (2.29 Ω), confirming improved electron transport efficiency (Fig. 3(c), Table S19).

ECSA, assessed via C_{dl} (Figs. 3(d) and S13) [36], reveals a higher C_{dl} for HE-APOs-18 (2.52 mF cm^{-2}) than HE-APOs-12 (0.90 mF cm^{-2}). This increase suggests a greater number of exposed active sites due to O_v modulation. Moreover, intrinsic activity normalized by ECSA (Fig. 3(e)) further corroborates the superior catalytic performance of HE-APOs-18. Therefore, HE-APOs-18 outperforms not only HE-APOs-12 and IrO_2 but also other alkaline OER electrocatalysts. When compared to reported high-entropy catalysts, HE-APOs-18 demonstrates lower overpotentials, underscoring its exceptional performance in alkaline OER (Fig. 3(f), Table S20).

To evaluate the industrial potential of HE-APOs-18 for seawater electrolysis, their OER performance was compared with that of HE-APOs-12 in both alkaline simulated seawater (1.0 M KOH + 0.5 M NaCl) and alkaline natural seawater (1.0 M KOH + seawater) electrolytes. In the 1.0 M KOH + 0.5 M NaCl solution, HE-APOs-18 exhibits superior catalytic activity, achieving current densities of 10 and 100 mA cm^{-2} at overpotentials of 243 and 277 mV, respectively, compared to 280 and 340 mV for HE-APOs-12 (Fig. S14). The Tafel slope of HE-APOs-18 (35.7 mV dec^{-1}) is significantly lower than that of HE-APOs-12 (65.4 mV dec^{-1}), indicating faster kinetics (Fig. S15). EIS measurements (Fig. S16, Table S19) confirm a lower R_{ct} for HE-APOs-18, while C_{dl} values (Figs. S17 and S18) suggest a

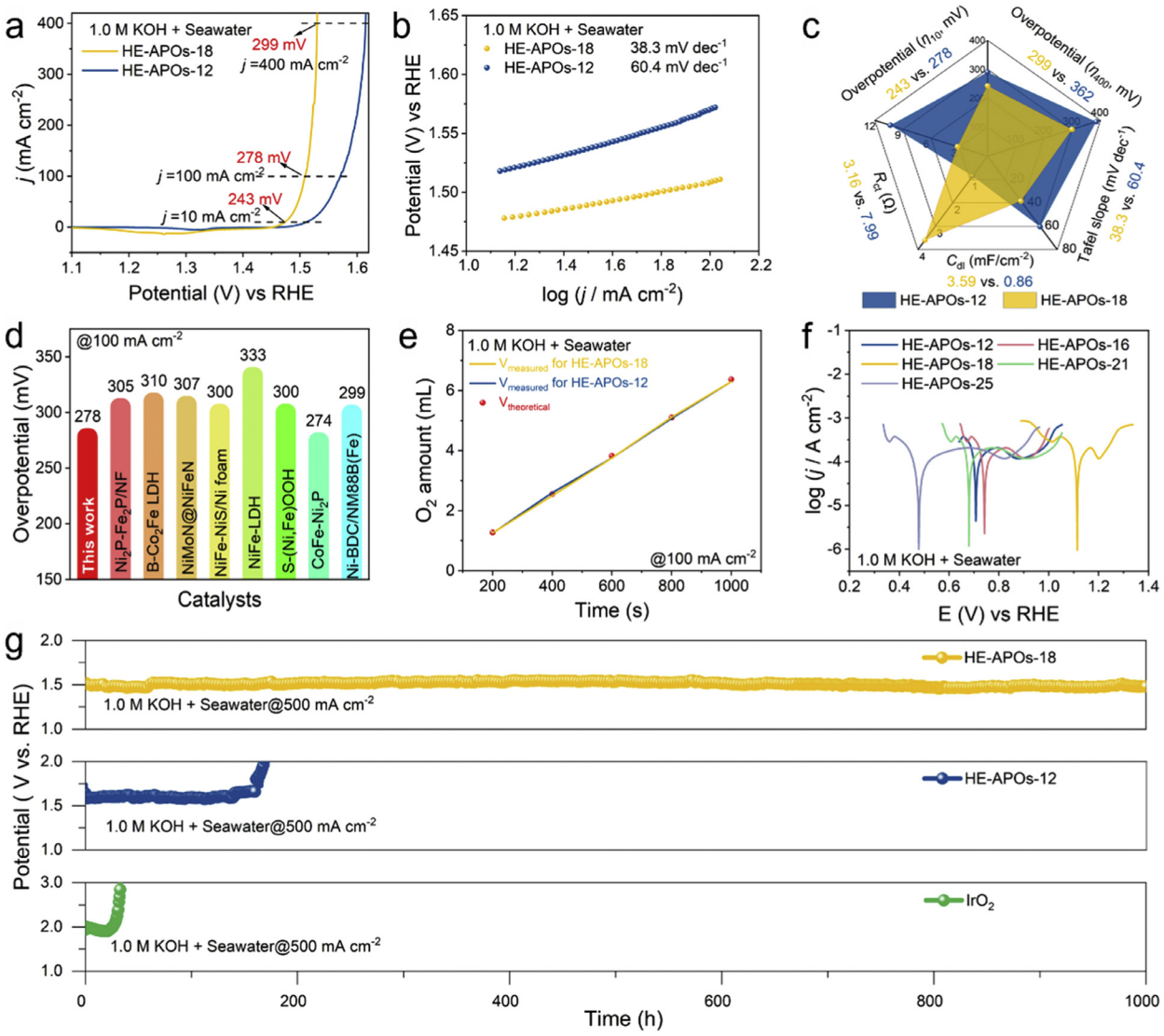

Fig. 4. Electrocatalytic OER performance of HE-APOs-18 and HE-APOs-12 samples in 1.0 M KOH + Seawater solution. (a) LSV curves and (b) Tafel slopes. (c) Comprehensive comparisons of the OER performance of HE-APOs-12 and HE-APOs-18. (d) The overpotential of HE-APOs-18 compared to other reported materials at 100 mA cm^{-2}. (e) Faraday effective. (f) Corrosion polarization curves. (g) Chronoamperometry *i*–*t* curves of HE-APOs-18, HE-APOs-12, and IrO_2.

higher density of active sites, highlighting their strong potential as seawater electrocatalysts.

In alkaline natural seawater, HE-APOs-18 maintains comparable activity, delivering 10 and 400 mA cm^{-2} at overpotentials of 243 and 299 mV, respectively, outperforming commercial catalysts (Fig. 4(a and c)). HE-APOs-18 also exhibits the lowest Tafel slope (38.3 mV dec^{-1}) and R_{ct} (3.16 Ω) compared to HE-APOs-12 (60.4 mV dec^{-1}, 7.99 Ω) (Figs. 4(b and c) and S19 and Table S19). The generation of O_v increases the number of active sites, as confirmed by the C_{dl} results (Figs. S20 and S21). Moreover, the TOF analysis under alkaline natural seawater electrolysis (Fig. S22) reveals that HE-APOs-18 possesses a much higher TOF across the whole overpotential range than HE-APOs-12, further confirming its superior intrinsic activity. Consequently, HE-APOs-18 emerges as a top-tier seawater OER catalyst (Fig. 4(d), Table S21), achieving high Faradaic efficiency (approximately 98.8%), with O_2 volumes matching theoretical values (Figs. S23 and 4(e)).

To elucidate the origin of the catalyst's superior stability, we systematically investigated the influence of O_v concentration on its resistance to chloride corrosion. Corrosion polarization curves were measured for catalysts with varying O_v levels, including HE-APOs-12, -16, -18, -21, and -25 (Fig. 4(f)). The key corrosion parameters, including corrosion potential (E_{corr}) and corrosion current density (j_{corr}), are summarized in Table S22. A clear volcano-type relationship is observed, with HE-APOs-18 exhibiting the highest E_{corr} and the lowest j_{corr}, indicating its optimal resistance to chloride corrosion. Specifically, as the O_v concentration increased from 12% to 18%, the corrosion resistance was significantly enhanced. However, a further increase in O_v concentration to 21% and 25% led to a notable decline in corrosion resistance. This trend suggests that while a moderate O_v concentration is crucial for inducing the protective high-spin state, excessive vacancies might compromise the material's structural integrity, creating defect sites that are susceptible to corrosive attack.

This finding was strongly corroborated by our long-term stability tests conducted at an industrial-scale current density of 500 mA cm^{-2}. As shown in the corrected Figs. 4(g) and S24, the operational durability of the catalysts directly correlates with their corrosion resistance. HE-APOs-18 demonstrates exceptional stability, maintaining a remarkably steady operating potential for over 1000 h. In contrast, catalysts with both lower (HE-APOs-12) and significantly higher (HE-APOs-25) oxygen vacancy concentrations

exhibit much poorer long-term durability. Specifically, HE-APOs-12 degrades rapidly after only 160 h of operation, while HE-APOs-25 also shows poor stability, underscoring the critical importance of an optimal oxygen vacancy concentration for achieving robust performance.

To further verify the inhibition of the competitive chlorine evolution reaction, a DPD colorimetric assay was performed on the electrolyte to detect hypochlorite (ClO^-) following 100 h of high-current-density operation. UV-vis spectroscopic analysis confirms that no ClO^- is formed (Figs. S25 and S26), which serves as direct chemical proof of the catalyst's exceptional robustness against chlorine-induced side reactions. Collectively, these systematic electrochemical data provided compelling evidence that our etching strategy, by precisely tuning the oxygen vacancy concentration to an optimal level (around 18%), was the key to simultaneously enhancing the intrinsic corrosion resistance and achieving exceptional long-term operational stability in seawater electrolysis. Building on these promising results, future investigations will be crucial to address its ultimate long-term phase stability, potential metal leaching under pilot-scale conditions, and the engineering challenges of scalable production, thereby bridging the gap between laboratory-scale success and industrial viability.

3.3. Reaction kinetics and surface reconstruction

To further investigate charge transfer kinetics, Operando EIS was conducted. At lower voltages (1.20–1.40 V), the EIS spectra of HE-APOs-18 exhibit near-vertical lines, indicative of high R_{ct} (Fig. S27). At 1.45 V, a distinct semicircle emerges, signaling the onset of OER. HE-APOs-12 displays a similar trend but with a larger R_{ct}, confirming its slower reaction kinetics and inferior electron transport compared to HE-APOs-18. Bode-phase plots (Fig. 5(a and b)) reveal phase angle shifts across frequencies, with intermediate frequency angles corresponding to inner-layer electron transport and low-frequency angles to surface electron transfer. HE-APOs-18 exhibits smaller phase angles at both frequencies, indicating enhanced electron transport and an earlier OER onset.

In-situ Raman spectroscopy provides further insights into the role of O_v in accelerating surface reconstruction (Fig. 5(c and d)). A peak at 577 cm^{-1}, indicative of oxy-hydroxide formation, appears at 1.30 V for HE-APOs-18 but is delayed to 1.40 V for HE-APOs-12, suggesting a more facile activation process. Crucially, this oxy-hydroxide peak in HE-APOs-18 remains stable in position across the entire potential window up to 1.60 V. In stark contrast, the corresponding peak for HE-APOs-12 exhibits a sharp blue-shift at 1.60 V, a spectroscopic fingerprint of uncontrolled over-oxidation and structural instability under high anodic stress [37]. This stark difference in structural evolution is attributed to the protective, high-spin-induced hydrogen-bonded water network on the HE-APOs-18 surface, which shields the active sites from direct exposure to the harsh electrochemical environment, unlike the unprotected surface of HE-APOs-12. This observation provides direct evidence that the spin-engineered HE-APOs-18 possesses superior structural robustness, which is fundamental to its enhanced durability. Furthermore, FeOOH peak analysis reveals a higher proportion in HE-APOs-18 (Fig. S28), suggesting stronger bonding between four-coordinated Fe and oxygen intermediates [38]. H_2O stretching bands (Fig. 5(e and f)) are deconvoluted into three peaks: ~3238 cm^{-1} (4HB-H_2O), ~3433 cm^{-1} (2HB-H_2O), and ~3586 cm^{-1} (K^+-H_2O). For HE-APOs-12, K^+-H_2O and 4HB-H_2O contents remain relatively unchanged (Table S23), whereas in HE-APOs-18, K^+-H_2O content decreases from 12.1% to 6.0%, while 4HB-H_2O increases from 44.3% to 56.6% as potential rose from 0 to 1.60 V (Table S24) [39,40]. This suggests that O_v-induced high-spin states facilitate K^+-H_2O desolvation, forming a robust hydrogen-bonding network that enriches hydroxide ions, enhancing Cl^- corrosion resistance and stability.

After a 24-h chronopotentiometry test, HE-APOs-18 retain their amorphous structure and surface roughness (Figs. S29 and S30). HRTEM reveals surface lattice fringes consistent with crystalline or semi-crystalline oxy-hydroxide formation (Fig. S30(c)), while the bulk structure remains amorphous [41,42] (Fig. S30(d)). EDX mapping confirms uniform elemental distribution (Fig. S30(e)). To further probe the compositional integrity, post-OER ICP analysis was performed. The results (Fig. S31) show that the bulk elemental composition remains consistent with the as-synthesized catalyst, confirming its excellent resistance to elemental leaching during the stability test. Remarkably, this structural robustness was maintained even after the extended 1000-h stability test. As shown in the post-operational SEM image in Fig. S32, the initial rod-like morphology is largely preserved beneath a layer of reconstructed nanoparticles, providing powerful evidence for the catalyst's exceptional corrosion resistance under prolonged operation.

XPS analysis (Fig. 5(g–i)) shows oxidation of Fe^{2+} to Fe^{3+}, Ni^{2+} to Ni^{3+}, and Co^{2+} to Co^{3+}, with Mn shifting to higher oxidation states (Fig. S33(a)). The O 1*s* spectra reveal an increase in surface hydroxyls (Fig. S33(b)), indicating strong $^*OH$ enrichment. P 2*p* spectra confirm the presence of phosphorus species on both HE-APOs-18 and HE-APOs-12 (Fig. S33(c and d)), suggesting that the excellent catalyst stability is weakly correlated with phosphorus species, challenging the conventional assumption that P-induced surface anion repulsion of Cl^- governs stability [43,44].

3.4. Mechanistic insights into HE-APOs' electrocatalytic enhancement via theoretical calculations

DFT calculations were performed to elucidate the mechanisms underlying the enhanced electrocatalytic performance of optimized HE-APOs. To systematically investigate the effect of oxygen vacancy concentration on the catalyst, we constructed four models: HE-APOs-pri (no O_v), HE-APOs-12 (12% O_v), HE-APOs-18 (18% O_v), and HE-APOs-25 (25% O_v). Details of the model constructions with varying Fe coordination numbers, based on EXAFS and XRD results (Figs. 2(f) and S34, Table S18), are provided in the experimental section and illustrated in Fig. S35. Gibbs free energy (ΔG) calculations for the four OER steps across different metal sites identified the $^*OH \rightarrow {}^*O$ transformation as the rate-determining step (RDS) for Fe, Ni, and Mn, while for Co, the RDS was $^*O \rightarrow {}^*OOH$ (Fig. 6(a and b)). O_v regulation reduced ΔG_{RDS} for Fe, Co, Ni, and Mn sites from 2.02, 2.22, 2.18, and 2.11 eV (HE-APOs-pri) to 1.76, 1.81, 2.09, and 1.85 eV (HE-APOs-18), respectively, with Fe achieving a $\Delta G_{O^*} - \Delta G_{OH^*}$ value closest to the theoretical optimum of 1.60 eV, demonstrating that Fe is the primary active site, consistent with the experimental results presented earlier.

As shown in Fig. 6(c), increasing the O_v concentration initially lowers ΔG_{RDS} for the Fe sites, but this effect diminishes at higher O_v levels, aligning with experimental results. This suggests that moderate O_v effectively reduces the RDS energy barrier and enhances OER kinetics by altering Fe coordination number. In addition, spin-state correlation analysis of ΔG (Fig. S36) reveals that Fe sites experience a reduction in ΔG_{RDS} when modulated to high-spin states. This finding underscores the critical interplay between O_v modulation, spin state optimization, and the enhanced OER performance.

To gain further insights into the decreased ΔG_{RDS}, an analysis of Fe-O bonding revealed a progressive strengthening of Fe-O bonds with the increment of O_v concentration. Specifically, the integrated crystal orbital Hamilton population (COHP) values for Fe-O bonding increase from 0.72 in HE-APOs-pri to 5.29 in HE-APOs-25 (Figs. 6(d) and S37). It is also necessary to note that excessive O_v leads to over adsorption, which hinders product desorp-

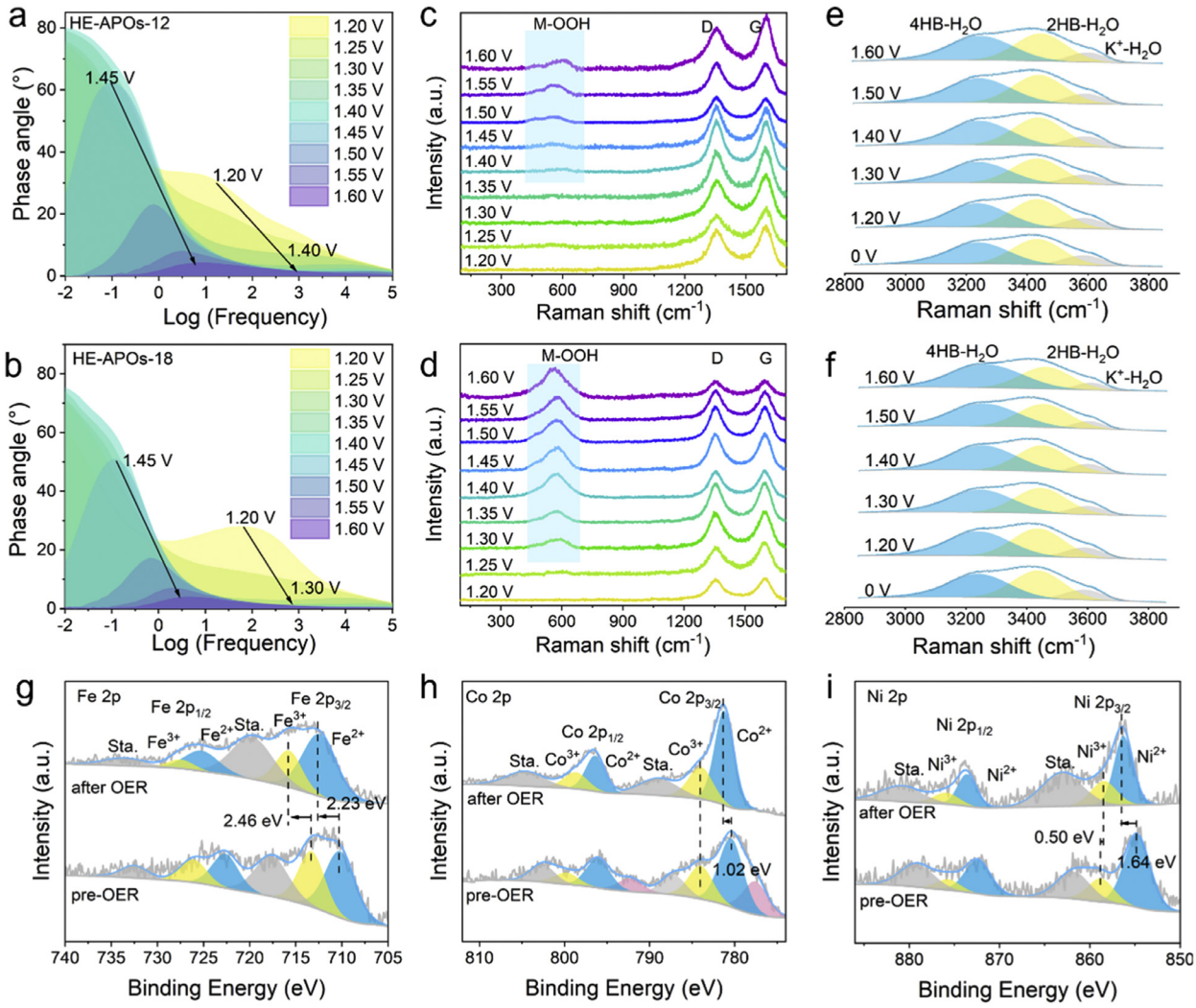

Fig. 5. Operando Bode-phase plots of HE-APOs-12 (a) and HE-APOs-18 (b) under different operated potentials (vs RHE). In-situ Raman spectra of HE-APOs-12 (c) and HE-APOs-18 (d). In-situ Raman spectra of interfacial water at HE-APOs-12 (e) and HE-APOs-18 (f). The 4HB-H_2O, 2HB-H_2O, and K^+-H_2O present three kinds of O-H stretching modes for H_2O. High-resolution XPS spectra of Fe 2*p* (g), Co 2*p* (h), Ni 2*p* (i).

tion and reduces overall catalytic efficiency [45]. Electron localization function (ELF) and Bader charge analyses (Figs. S38 and 6(e)) reveal that moderate O_v levels delocalize electrons around Fe to O, thus strengthening the Fe-O bonds, while excessive O_v causes severe localization and low activity [46]. Density of states (DOS) analysis (Figs. S39 and S40) demonstrates that O_v-induced symmetry breaking causes significant alterations in the Fe-centered crystal field [47,48]. For instance, total DOS (TDOS) comparisons reveal pronounced orbital splitting in HE-APOs-18, while projected DOS (PDOS) indicates enhanced contributions from higher-energy Fe 3*d* states due to electrons released from O_v formation. As a result, an increase in π-bonding between Fe and *O intermediates was found (Figs. 6(d) and S41) [49]. Given that the Fe sites show strong spin polarization, O_v-induced spin polarization enhances spin matching between metal ions and reaction intermediates, as revealed below [50].

To evaluate the impact of O_v on stability during seawater electrolysis, COHP, adsorption energy analyses, and ELF were employed. COHP analysis of Fe bonding with adsorbed species (Fig. S42) highlights significantly stronger Fe-OH bonding compared to Fe-Cl, which is consistent with adsorption energy calculations, i.e., Fe sites exhibit a higher affinity for *OH over *Cl (Fig. 6(f)), which is critical for long-term durability. Comparison of Fe-OH bonding strengths between HE-APOs-pri and HE-APOs-18 further revealed enhanced bonding with *OH across all metal sites in HE-APOs-18 compared to HE-APOs-pri due to O_v modulation, suggesting that O_v-induced high-spin states promote *OH enrichment and the formation of a hydrogen-bonded water network on the surface. As supported by ELF analysis, unpaired valence electrons at Fe sites facilitate hydrogen-bonding interactions with interfacial water molecules, effectively repelling chloride ions due to charge mismatch (Fig. 6(g)).

Experimentally, a strong correlation between spin states and catalytic performance suggests that OER activity can be effectively modulated by tuning the O_v concentration (Fig. 6(h)). The calculated magnetic moments for each structure, including total and site-specific magnetization of transition metals, are presented in Figs. 6(e) and S43. A progressive increase in magnetic moments is observed, rising from 26.89 μ_B (HE-APOs-pri) to 33.72 μ_B (HE-APOs-12), 39.02 μ_B (HE-APOs-18), and slightly decreasing to 37.02 μ_B (HE-APOs-25), confirming that oxygen vacancies effectively enhance the spin state of HE-APOs-pri [51]. The presence of net magnetic moments facilitates superexchange interactions among transition metal ions. As shown in Figs. 6(i) and S44, spin density and magnetic exchange analyses revealed strong coupling among Fe^{3+}-O^{2-}-Co^{2+} and Ni^{2+}-O^{2-}-Mn^{4+} linkages, underscoring the critical

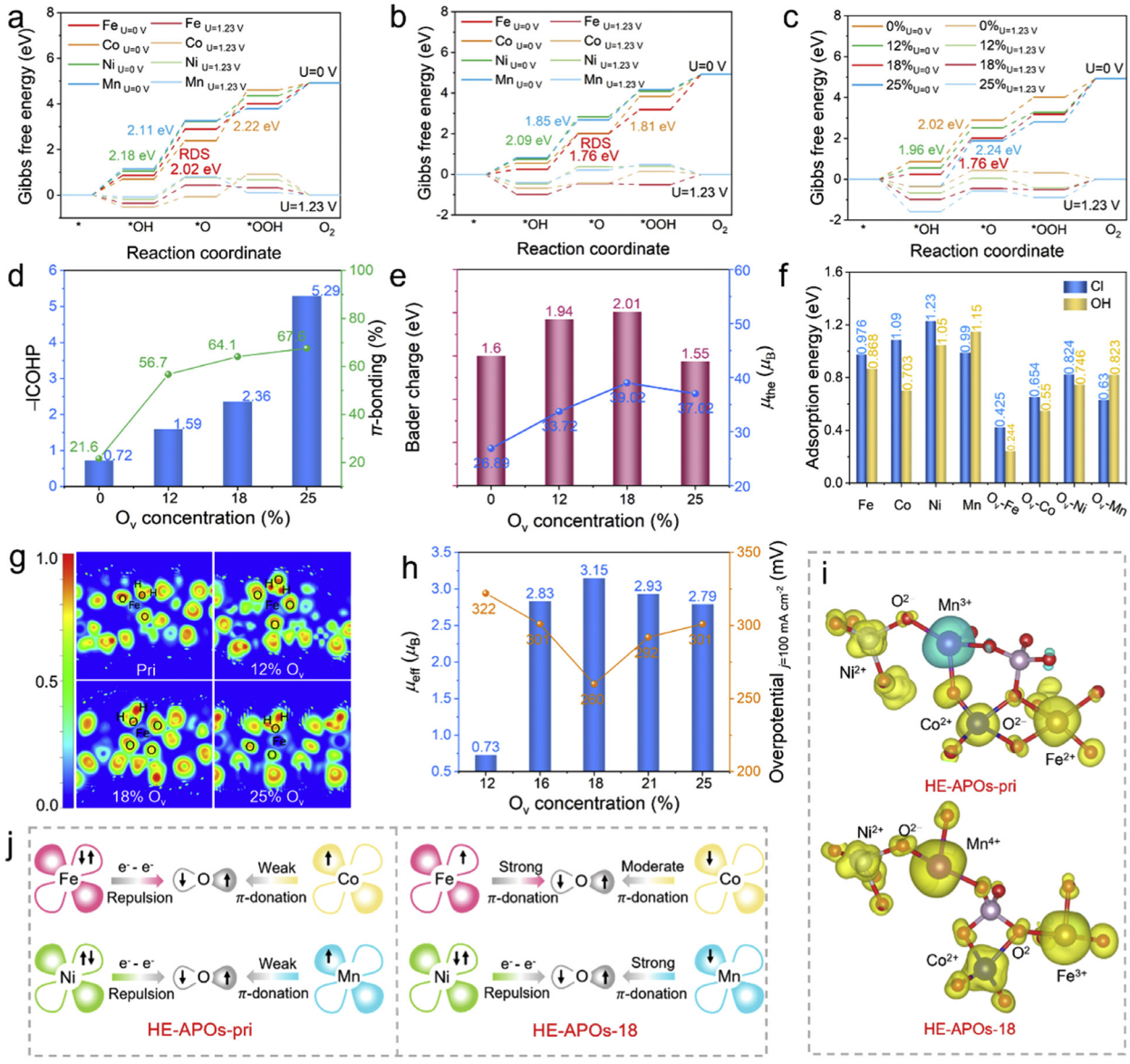

Fig. 6. Intrinsic mechanism of O_v optimization OER performance using DFT analysis. ΔG step diagram during the OER process of HE-APOs-pri (a), HE-APOs-18 (b), and Fe site with varying O_v concentrations (c). (d) Relationship between O_v concentration, integrated COHP (ICOHP), and π-bonding contributions. (e) Correlation between O_v concentration, Bader charge of Fe atom, and theoretical magnetic moment. (f) Adsorption energy comparisons between different metal sites in HE-APOs-pri and HE-APOs-18 with adsorbed species (*OH and *Cl). (g) ELF calculations for H_2O adsorption on the Fe atom. (h) Correlation between O_v concentration, effective magnetic moment, and OER activity in 1.0 M KOH electrolyte. (i) 3D spin electron density maps. Blue and yellow denote spin up and spin down, respectively. (j) Schematic representations of the magnetic superexchange interaction among Fe, Co, Ni, and Mn in HE-APOs-pri and HE-APOs-18.

role of O^{2-} and O_v in modifying these interactions. The schematic in Fig. 6(i) illustrates these magnetic superexchange interactions in HE-APOs-pri and e-HE-APOs-18. Notably, Fe exhibits the strongest π-donation to bridging O^{2-} due to unpaired t_{2g}, Co and Mn show weaker e_g-based π-bonding, while Ni, with fully occupied d orbitals, experiences electronic repulsion from bridging O^{2-}, thereby limiting its interaction (Fig. 6(j)) [52,53].

The high-spin states of HE-APOs-18, induced by O_v, enable Fe sites to optimize their electronic structure via strengthened superexchange interactions. Since all key OER intermediates (*O, *OH, and *OOH) possess net spin moments, the increased magnetic moments of active Fe sites enhance their interaction with these intermediates. This facilitates the formation of an extensive hydrogen-bonded water network, which carries a negative charge and consequently repels Cl^- species. Such an effect not only boosts the catalytic activity but also significantly enhances the long-term stability of HE-APOs-18 in seawater electrolysis.

4. Conclusions

In this study, we demonstrated an advanced catalyst, HE-APOs, for seawater electrolysis with excellent catalysis performance and durability. The key is to engineer the spin states of the transition metal center mediated by oxygen vacancies. Specifically, the optimized spin electrocatalyst achieved a low overpotential of 299 mV at 400 mA cm^{-2} and demonstrated excellent long-term stability of over 1000 h at 500 mA cm^{-2} in alkaline seawater. Turning oxygen vacancy can generate four-coordinated $FeCoNiMnPO_x$ exhibited the highest spin-state transitions, which enhanced magnetic superexchange interactions and optimized π-bonding with oxygen intermediates. Such tuning led to a near-ideal OER activity descriptor value of $\Delta G_{O^*} - \Delta G_{OH^*} = 1.76$ eV, which not only selectively improved the intermediate adsorption but also facilitated the accumulation of hydroxide ions, in turn repelling chloride ions to achieve long-term stability. Our work paves the way for designing

advanced high-entropy electrocatalysts with molecular-level selectivity for efficient and durable seawater oxidation via spin-state engineering.

Declaration of competing interest

The authors declare that they have no known competing financial interests or personal relationships that could have appeared to influence the work reported in this paper.

CRediT authorship contribution statement

Hai Li: Writing – review & editing, Writing – original draft, Project administration, Investigation, Funding acquisition, Formal analysis, Data curation, Conceptualization. **Mingyu Wang:** Writing – review & editing, Validation, Supervision, Software, Resources, Conceptualization. **Xiaoliang Zhang:** Writing – review & editing, Methodology, Formal analysis, Data curation. **Wen-Qiang Xie:** Writing – review & editing, Supervision, Software, Methodology, Data curation, Conceptualization. **Hongliang Dong:** Writing – review & editing, Resources. **Yangyang Liu:** Methodology, Formal analysis, Data curation. **Youpeng Li:** Methodology, Formal analysis. **Yifeng Wang:** Methodology, Formal analysis. **Zhun Tang:** Methodology, Formal analysis. **Rongbin Lin:** Methodology, Formal analysis. **Aimin Yu:** Resources. **Dong-Sheng Li:** Resources, Conceptualization. **Weiwei Li:** Writing – review & editing, Writing – original draft, Resources, Methodology, Investigation, Formal analysis, Data curation, Conceptualization. **Chenghua Sun:** Writing – review & editing, Software, Methodology. **Jinchun Tu:** Writing – review & editing, Resources, Investigation, Funding acquisition, Data curation, Conceptualization.

Acknowledgments

This study was financially supported by the National Natural Science Foundation of China (Nos. 12304060, 52562009, and 22566018), the Hainan Provincial Natural Science Foundation of China (Nos. 222QN222 and 225QN214), the Hainan Province Science and Technology Special Fund of China (No. ZDKJ2021029), and the Innovative Scientific Research Project of Hainan Province for Graduate Students (Qhyb2023-51). We thank the staff of the BL17B beamline (https://cstr.cn/31129.02.NFPS.BL17B) at the National Facility for Protein Science in Shanghai (NFPS, https://cstr.cn/31129.02.NFPS), Shanghai Advanced Research Institute, Chinese Academy of Sciences, for their technical support in Single-crystal XAFS data collection and analysis.

Supplementary materials

Supplementary material associated with this article can be found, in the online version, at doi:10.1016/j.jmst.2025.09.047.

References

[1] L. Zhou, D. Guo, L. Wu, Z. Guan, C. Zou, H. Jin, G. Fang, X.A. Chen, S. Wang, Nat. Commun. 15 (2024) 2481.
[2] Y. Bao, H. Ru, Y. Wang, K. Zhang, R. Yu, Q. Wu, A. Yu, D.S. Li, C. Sun, W. Li, Adv. Funct. Mater. 34 (2024) 2314611.
[3] X. Duan, Q. Sha, P. Li, T. Li, G. Yang, W. Liu, E. Yu, D. Zhou, J. Fang, W. Chen, Nat. Commun. 15 (2024) 1973.
[4] J. Liu, S. Duan, H. Shi, T. Wang, X. Yang, Y. Huang, G. Wu, Q. Li, Angew. Chem. Int. Ed. 61 (2022) e202210753.
[5] Y. Kuang, M.J. Kenney, Y. Meng, W.H. Hung, Y. Liu, J.E. Huang, R. Prasanna, P. Li, Y. Li, L. Wang, M.C. Lin, M.D. McGehee, X. Sun, H. Dai, Proc. Natl. Acad. Sci. U. S. A. 116 (2019) 6624–6629.
[6] A.K. Ipadeola, S. Mathi, M.H. Sliem, M.-S. Balogun, A.M. Abdullah, J. Mater. Chem. A 13 (2025) 22200–22239.
[7] Y. Xie, S. Xu, A.C. Meng, B. Zheng, Z. Chen, J.M. Tour, J. Lin, Energy Environ. Sci. 17 (2024) 8682–8670.
[8] J. Liang, Z. Li, X. He, Y. Luo, D. Zheng, Y. Wang, T. Li, B. Ying, S. Sun, Z. Cai, Mater. Today 69 (2023) 193–235.
[9] X. Wang, H. Hu, J. Song, J. Ma, H. Du, J.J. Wang, M. Wang, W. Chen, Y. Zhou, J. Wang, Adv. Energy Mater. 15 (2025) 2402883.
[10] J. Chang, G. Wang, Z. Yang, B. Li, Q. Wang, R. Kuliiev, N. Orlovskaya, M. Gu, Y. Du, G. Wang, Adv. Mater. 33 (2021) 2101425.
[11] Y. Li, S. Zuo, Q. Li, H. Huang, X. Wu, J. Zhang, H. Zhang, J. Zhang, Appl. Catal. B-Environ. Energy 318 (2022) 121832.
[12] D. Liu, X. Wei, J. Lu, X. Wang, K. Liu, Y. Cai, Y. Qi, L. Wang, H. Ai, Z. Wang, Adv. Mater. 36 (2024) 2408982.
[13] S. Gong, Y. Meng, Z. Jin, H.-Y. Hsu, M. Du, F. Liu, ACS Catal. 14 (2024) 14399–14435.
[14] M. Tu, Z. Zhu, Y. He, S. Mathi, J. Deng, M. Naushad, Y. Huang, Y.W. Hu, M.S. Balogun, Small 21 (2025) 2500687.
[15] J.W. Yeh, S.K. Chen, S.J. Lin, J.Y. Gan, T.S. Chin, T.T. Shun, C.H. Tsau, S.Y. Chang, Adv. Eng. Mater. 6 (2004) 299–303.
[16] Y. Zhai, X. Ren, B. Wang, S. Liu, Adv. Funct. Mater. 32 (2022) 2207536.
[17] M. Li, X. Wang, K. Liu, H. Sun, D. Sun, K. Huang, Y. Tang, W. Xing, H. Li, G. Fu, Adv. Mater. 35 (2023) e2302462.
[18] Z. Guo, Q. Zhu, S. Wang, M. Jiang, X. Fan, W. Zhang, M. Han, X. Wu, X. Hou, Y. Zhang, Angew. Chem. Int. Ed. 63 (2024) e202406711.
[19] K. Miao, W. Jiang, Z. Chen, Y. Luo, D. Xiang, C. Wang, X. Kang, Adv. Mater. 36 (2024) e2308490.
[20] R. Gond, S. Singh, X. Zhao, D. Singh, R. Ahuja, M. Fichtner, P. Barpanda, ACS Appl. Mater. Interfaces 14 (2022) 40761–40770.
[21] C. Xia, Y. Li, M. Je, J. Kim, S.M. Cho, C.H. Choi, H. Choi, T.-H. Kim, J.K. Kim, Nano Micro Lett. 14 (2022) 209.
[22] O.F. Ikotun, N. Marino, P.E. Kruger, M. Julve, R.P. Doyle, Coord. Chem. Rev. 254 (2010) 890–915.
[23] B. Ravel, M. Newville, J. Synchrotr. Radiat. 12 (2005) 537–541.
[24] S. Xu, S. Feng, Y. Yu, D. Xue, M. Liu, C. Wang, K. Zhao, B. Xu, J.N. Zhang, Nat. Commun. 15 (2024) 1720.
[25] M.-L. Guo, Z.-Y. Wu, M.-M. Zhang, Z.-J. Huang, K.-X. Zhang, B.-R. Wang, J.-C. Tu, Rare Metals 42 (2023) 1847–1857.
[26] Y. Hu, M. Tu, T. Xiong, Y. He, M. Mushtaq, H. Yang, Z. Khanam, Y. Huang, J. Deng, M.S. Balogun, J. Energy Chem. 103 (2025) 282–293.
[27] Z. Zhu, M. Tu, Y.W. Hu, W. Gan, J. Deng, Z. Wang, M.S. Balogun, J. Energy Chem. 108 (2025) 272–285.
[28] G. Kresse, D. Joubert, Phys. Rev. B 59 (1999) 1758.
[29] J.P. Perdew, K. Burke, M. Ernzerhof, Phys. Rev. Lett. 77 (1996) 3865.
[30] Z. Li, L. Deng, I.A. Kinloch, R. Young, Prog. Mater. Sci. 135 (2023) 101089.
[31] M. Del Nero, C. Galindo, R. Barillon, E. Halter, B. Madé, J. Colloid. Interface Sci. 342 (2010) 437–444.
[32] J. Hu, T. Guo, X. Zhong, J. Li, Y. Mei, C. Zhang, Y. Feng, M. Sun, L. Meng, Z. Wang, B. Huang, L. Zhang, Z. Wang, Adv. Mater. 36 (2024) e2310918.
[33] X. Li, T. Wu, N. Li, S. Zhang, W. Chang, J. Chi, X. Liu, L. Wang, Adv. Funct. Mater. 34 (2024) 2400734.
[34] D. Ji, L. Fan, L. Tao, Y. Sun, M. Li, G. Yang, T.Q. Tran, S. Ramakrishna, S. Guo, Angew. Chem. Int. Ed. 58 (2019) 13840–13844.
[35] S. Zhou, X. Miao, X. Zhao, C. Ma, Y. Qiu, Z. Hu, J. Zhao, L. Shi, J. Zeng, Nat. Commun. 7 (2016) 11510.
[36] B. Zhang, W. Li, K. Zhang, J. Gao, Y. Cao, Y. Cheng, D. Chen, Q. Wu, L. Ding, J. Tu, J. Mater. Sci. Technol. 177 (2024) 214–223.
[37] J. Huang, H. Sheng, R.D. Ross, J. Han, X. Wang, B. Song, S. Jin, Nat. Commun. 12 (2021) 3036.
[38] M. Cai, Q. Zhu, X. Wang, Z. Shao, L. Yao, H. Zeng, X. Wu, J. Chen, K. Huang, S. Feng, Adv. Mater. 35 (2023) 2209338.
[39] Y. Yan, J. Lin, K. Huang, X. Zheng, L. Qiao, S. Liu, J. Cao, S.C. Jun, Y. Yamauchi, J. Qi, J. Am. Chem. Soc. 145 (2023) 24218–24229.
[40] N. Yao, G. Wang, H. Jia, J. Yin, H. Cong, S. Chen, W. Luo, Angew. Chem. Int. Ed. 134 (2022) e202117178.
[41] X. Luo, P. Ji, P. Wang, X. Tan, L. Chen, S. Mu, Adv. Sci. 9 (2022) 2104846.
[42] J. Yue, Y. Li, C. Yang, W. Luo, Angew. Chem. Int. Ed. 137 (2025) e202415447.
[43] H. Zhang, Z. Bi, P. Sun, A. Chen, T. Wågberg, X. Hu, X. Liu, L. Jiang, G. Hu, ACS Nano 17 (2023) 16008–16019.
[44] H. Lv, Y. Gao, D.S. Li, A. Yu, C. Sun, C. Zhang, Adv. Funct. Mater. 35 (2024) 2418334.
[45] R. He, L. Yang, Y. Zhang, D. Jiang, S. Lee, S. Horta, Z. Liang, X. Lu, A. Ostovari Moghaddam, J. Li, M. Ibanez, Y. Xu, Y. Zhou, A. Cabot, Adv. Mater. 35 (2023) e2303719.
[46] S. Zhu, R. Yang, H.J.W. Li, S. Huang, H. Wang, Y. Liu, H. Li, T. Zhai, Angew. Chem. Int. Ed. 63 (2024) e202319462.
[47] X. Gu, M. Yu, S. Chen, X. Mu, Z. Xu, W. Shao, J. Zhu, C. Chen, S. Liu, S. Mu, Nano Energy 102 (2022) 107656.
[48] Y. Sun, W. Fan, Y. Li, N.L. Sui, Z. Zhu, Y. Zhou, J.M. Lee, Adv. Mater. 36 (2024) 2306687.
[49] Q. Jing, Z. Mei, X. Sheng, X. Zou, Q. Xu, L. Wang, H. Guo, Adv. Funct. Mater. 34 (2024) 2307002.
[50] Y. Sun, S. Sun, H. Yang, S. Xi, J. Gracia, Z. Xu, Adv. Mater. 32 (2020) 2003297.
[51] J. Zheng, G. Teng, C. Xin, Z. Zhuo, J. Liu, Q. Li, Z. Hu, M. Xu, S. Yan, W. Yang, F. Pan, J. Phys. Chem. Lett. 8 (2017) 5537–5542.
[52] J.Y.C. Chen, L. Dang, H. Liang, W. Bi, J.B. Gerken, S. Jin, E.E. Alp, S.S. Stahl, J. Am. Chem. Soc. 137 (2015) 15090–15093.
[53] J. Jiang, F. Sun, S. Zhou, W. Hu, H. Zhang, J. Dong, Z. Jiang, J. Zhao, J. Li, W. Yan, Nat. Commun. 9 (2018) 2885.